20th Australasian Fluid Mechanics Conference
Perth, Australia
5-8 December 2016

The transition to fully 3D chaos in Wavy Taylor Vortex flow

M. Rudman[1], M.F.M. Speetjens[2] and B. Ravu[3]

[1]Department of Mechanical and Aerospace Engineering, Monash University, Victoria 3800, Australia

[2]Department of Mechanical Engineering, Technische Universiteit Eindhoven, 5600 MB, Nederland

[3]IITB-Monash Research Academy, Indian Institute of Technology Bombay, Powai 400076, India.

Abstract

Taylor Vortex Flow (TVF) has only 2 degrees of freedom and the domain is fully foliated by Kolmogorov-Arnold-Moser (KAM) surfaces. Mixing thus only occurs via diffusion. For increasing Re TVF is replaced by wavy vortex flow (WVF) which has 3 degrees of freedom. WVF has the potential to exhibit chaotic advection which greatly enhances mixing. The rapid transition from TVF to WVF with increasing Reynolds number is known, however details of the transition are unclear. We introduce a new method for divergence-free interpolation of discrete velocity data and demonstrate how it improves the quality of the predicted Lagrangian flow structures. We show that the WVF perturbation primarily affects the inflow vortex boundary and acts to introduce chaos in the "outer" KAM tori. As the perturbation increases, more of the original KAM tori are destroyed, however new families of tori emerge from the chaos. These encircle the original surfaces in a non-simply connected way and occur for perturbations that are far from small. As the perturbation increases, the new KAM tori likewise succumb to a similar process of destruction until the flow is completely chaotic. This behaviour is essentially the same as exhibited by 2D unsteady incompressible flows. It implies that the 3D steady WVF flow can in a dynamic sense be seen as a composition of Hamiltonian systems that each correspond to a family of KAM tori and its local environment. This is consistent with the fact that 3D steady flows admit (local) expression as a Hamiltonian system in regions anywhere outside isolated stagnation points.

Introduction

The underlying essence of fluid chaos is that neighbouring points in a flow separate exponentially in time, resulting in exponential growth of material interfaces. In an incompressible flow, stretching in one direction necessarily implies contraction in another and this leads to finer structure that allows molecular diffusion to operate effectively. This basic mechanism is the one by which chaotic advection enhances mixing across many natural and industrial process [7]. Although turbulence is the mechanism that has most often been employed to generate mixing in practical applications, the idea that laminar, deterministic fluid flows can generate chaotic fluid trajectories is now understood and well-accepted.

Although the equation describing the motion of a fluid particle is simple, i.e. $d\boldsymbol{X}/dt=\boldsymbol{U}(\boldsymbol{X},t)$, the nature of the underlying velocity field is critical in determining whether the particle trajectories exhibit chaos. At a minimum, $\boldsymbol{U}(\boldsymbol{X},t)$ must have at least 3 degrees of freedom, either 2 spatial and time, or 3 spatial [8].

In the Lagrangian view of transport, the flow can be separated into topologically distinct regions, some of which admit chaotic motion and others that are integrable in the sense that they comprise of well defined "Lagrangian coherent structures" (LCSs) embedded in a higher-dimensional system (curves in 2D and especially surfaces in 3D). These LCSs are barriers to mixing and transport and an understanding of their creation & destruction provides information on the ability of a flow to admit chaos. The means by which these structures evolve with system parameters in 2D unsteady flows is well understood [8], however in 3D the picture is complex and less well known.

Taylor-Couette flow occurs between two concentric cylinders, and a plethora of different flow regimes exist depending on the ratio of inner to outer radius ($\eta=R_I/R_O$), the aspect ratio ($H/(R_I-R_O)$), the Reynolds numbers for the inner and outer cylinders (Re_I, Re_O) and the pathway of rotation rates (Ω_I, Ω_O) traversed to obtain the final values of (Re_I, Re_O) [1].

We consider inner cylinder rotation only, where cylindrical Couette flow is unstable to radial perturbations resulting in axisymmetric Taylor vortex flow (TVF). This flow consists of a set of stacked counter-rotating toroidal vortices. TVF does not admit chaos, and fluid particles are constrained to lie on surfaces of invariant toroidal surfaces ("KAM tori"). For increasing Re, TVF is unstable to azimuthal perturbations, leading to a fully 3D unsteady flow known as wavy vortex flow (WVF). It has been observed that WVF has the potential for chaotic advection [10]. There, the wave state was shown to have a significant affect on mixing. More fundamental was the observation that the transition from completely integrable axisymmetric flow to fully chaotic flow occurred over a small increment in Re. For the wave states examined in detail in [10], TVF is predicted [4] to become azimuthally unstable at around $Re_I = 143$. In [10] WVF at $Re_I = 162$ was predicted to be fully chaotic. The mechanisms responsible for this rapid transition are unknown and are the subject of this study.

Methodology

WVF is categorised by an axial wavelength λ_z (equal to the size of a pair of vortices) and an azimuthal wavenumber m. Here, we simulate a small section of a complete WVF in a computational domain with an axial extent of $Z = \lambda_z$ and an azimuthal extent of one wave (i.e. $\Theta = 2\pi/m$) (see [10] for details). This domain is doubly periodic and implicitly infinite in the axial direction. For a large aspect ratio apparatus this approximation is a good one away from the end walls. The flow field is determined using the spectral element-Fourier code *semtex* [3]. The wave period T is determined from the flow field and rotational velocity of the frame in which the flow appears steady is given by $\Omega_I = 2\pi/mT$.

All of the analysis undertaken below relies on the accurate prediction of fluid particle trajectories in the wave's rotating frame. (**NOTE**: for brevity, the word "particle" is used to mean "fluid particle"). In [10] an adaptive step size RK4 algorithm was used to integrate particle trajectories, with particle velocities interpolated from grid-velocities using tri-quadratic interpolation.

Although trajectories appeared reasonable, there was a non-physical "fuzziness" in the Poincaré sections indicating accumulated errors in long-time integration of trajectories. Although the shadowing lemma [6] suggests these errors will be primarily in the particle's position *on* an invariant surface (rather than errors normal to it), the fuzziness suggests that periodic points and lines as well as details of the flow near transition to chaos and in regions where small scale structure such as 'cantori' should be observed are not accurately predicted. In [9] we showed that the major source of error is the non-solenoidal property of the interpolated velocity field used in [10].

Divergence-free velocity field

Incompressibility implies a (locally) Hamiltonian structure for the equations of motion and thus accurately preserving the divergence-free nature of the flow is crucial for reliable numerical simulations. In [9] a new method was proposed that creates an analytically divergence-free velocity field from regularly gridded data. Based on a similar method by Finn and Chacon [5] it creates an analytic vector potential $\boldsymbol{A}$, the curl of which is (by construction) divergence-free, i.e. $\boldsymbol{V} = \boldsymbol{\nabla} \times \boldsymbol{A}$. We present a brief overview of the method here (details are in [9]).

In creating a suitable $\boldsymbol{A}$, there is a gauge freedom that allows us to set one component of the potential to zero. We choose A_z=0:

$$V_x = -\frac{\partial A_y}{\partial z}, \quad V_y = \frac{\partial A_x}{\partial z}, \quad V_z = \frac{\partial A_y}{\partial x} - \frac{\partial A_x}{\partial y}. \tag{1}$$

We now define $\boldsymbol{A}$ using B-splines. The 1D B-spline ϕ is given by

$$\phi(t) = \begin{cases} 4 - 6|t|^2 + 3|t|^3 & |t| < 1 \\ (2 - |t|)^3 & 1 \le |t| \le 2 \\ 0 & \text{otherwise} \end{cases} \tag{2}$$

Defining 1D basis functions (e.g. in the x-direction)

$$b_i(x) = \phi\left(\frac{x - x_0}{h_x} - i\right), \quad i = -1, \ldots, n_x + 1 \tag{3}$$

each component of $\boldsymbol{A}$ is written as a tensor product of 1D B-splines as (e.g. for A_x)

$$A_x(x,y,z) = \sum_{i=-1}^{n_x+1} \sum_{j=-1}^{n_y+1} \sum_{k=-1}^{n_z+1} c_{ijk}\, b_i(x) b_j(y) b_k(z) \tag{4}$$

The key difficulty is that in order to fit splines to the vector potential $\boldsymbol{A}$ we only have derivative information (i.e. the velocity field as specified in equation (1)). However, because the analytic derivative of the splines (equation (4)) are easily determined it is then possible to determine the spline coefficients c_{ijk} using (e.g.)

$$V_y = \frac{\partial A_x}{\partial z} = \sum_{i=-1}^{n_x+1} \sum_{j=-1}^{n_y+1} \sum_{k=-1}^{n_z+1} c_{ijk}\, b_i(x) b_j(y) \frac{\partial b_k(z)}{\partial z} \tag{5}$$

This approach allows A_x and A_y to be determined and the resulting (analytic) derivatives w.r.t. z will exactly return the x- and y-velocities on the grid. An analytic expression for the z-component of velocity is also provided by the third of equations (1). We have found that this component of velocity at the nodal points does not exactly match the original data, however the difference is typically order 10^{-6}. Most importantly, the resulting (analytic) velocity field is guaranteed to be analytically divergence-free by construction. This field is then used to integrate particle trajectories. A comparison between the new method and that of [10] is shown in Figure 1.

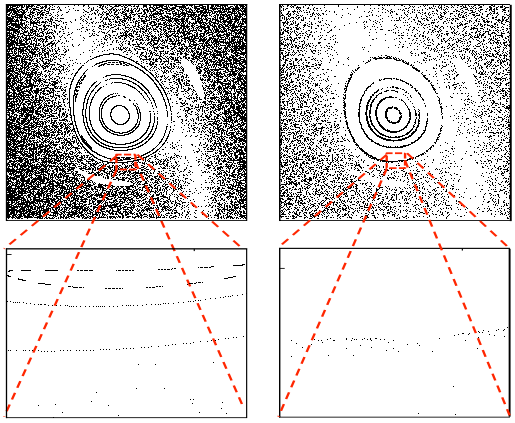

Figure 1. Poincaré sections for $Re = 155$ using the analytically divergence-free velocity field (left) and tri-quadratic interpolation from the grid data (right).

The Poincaré section is calculated using a 5th order Cash-Karp variable step Runge-Kutta method with adaptive time-step control and a tolerance of 10^{-10}. The ability of the new method to accurately track particles and identify periodic points and other fine-scale structure is clearly seen in Figure 1..

Results and Analysis

Velocity field prediction

We choose a domain that corresponds to a wave-state that exists for a large range of Re, $(m, \lambda_z) = (6, 2.325)$. We predict that this flow is axisymmetric at Re=153.5, and is wavy at Re=153.6. Simulations in the vicinity of this transition took very long times to converge and it was not feasible to calculate velocity fields using *semtex* between these two values of Re. Instead, we define a *perturbation flow* (PFL) as $\text{PFL} = \text{WVF}_{Re=153.6} - \text{TVF}_{Re=153.5}$. For flows with Re less than 153.6 we use an approximate WVF given by $\text{WVF} = \text{TVF}_{Re=153.5} + \varepsilon \times \text{PFL}$, and define these flows based on the value of ε we use. For flows above Re=153.6 we use the flow determined using *semtex*. In terms of velocity magnitude, the TVF vortex velocity is order 10% of the inner cylinder speed and the magnitude of the PFL velocity is order 10% of this (i.e. 1% of the inner cylinder speed). The periodicity, T, used for all such calculations is that for $\text{WVF}_{Re=153.6}$.

The perturbation flow determines the initial transition from an axisymmetric state, thus we define Φ_S that measures the proportional deviation of PFL from TVF as:

$$\Phi_S = \left(\frac{|u'|}{|\bar{u}|}\right)\left\{\frac{\pi}{2} - \text{abs}\left(\sin^{-1}\left(\frac{\bar{u}\cdot u'}{|\bar{u}||u'|}\right)\right)\right\} \tag{6}$$

Here u' is the perturbation velocity (PFL) and $\bar{u}$ is the TVF flow velocity. The distribution of Φ_S changes with azimuth, but the location of the peak value is shown in the centre image of Figure 2 alongside the magnitude of PFL (left) and contours of azimuthal velocity and in-plane vectors of the axisymmetric flow (right). Note that the maximum relative perturbation to the axisymmetric flow occurs at the outer cylinder on the inflow jet between vortices.

On some of the KAM tori in TVF a fluid particle will come back to the same point after one (or more) traverses of the domain – such points are known as periodic points and for TVF, if one point is periodic, all points on the same tori must also be periodic. These periodic KAM tori play an important role in the transition to chaos.

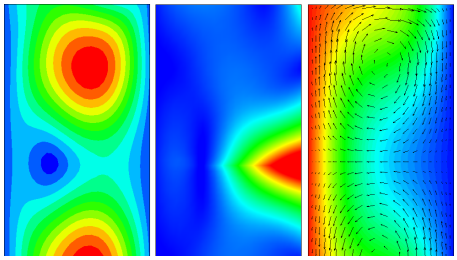

Figure 2. Contours of PFL magnitude (left), perturbation angle Φ_S (centre) and azimuthal velocity for axisymmetric TVF (right).

Transition from integrability

The transition from purely axisymmetric flow is shown in Figure 3 for $\varepsilon = 0.001$ and 0.1. The magnitude of the perturbation is order 0.01ε times the inner cylinder velocity (i.e. 10^{-5} times for $\varepsilon = 0.001$). Recalling Figure 2, the maximum perturbation to the flow (and hence the trajectories) occurs at the inflow boundary and it is regions associated with this that we expect to first deviate from integrability. This is seen in Figure 3a where the outer toroidal surfaces start to break up (these are "downstream" from the region of maximum perturbation and are most affected).

For $\varepsilon = 0.001$ the periodic KAM surfaces toward the outside of the vortices have started to break up, being replaced by trajectories that are "fuzzy" (red, dark blue). A 3D close-up of this case is also shown in Figure 4 in which Period-1 lines are also plotted.

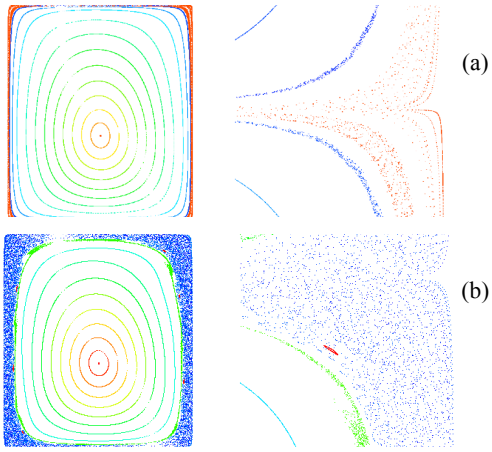

Figure 3. Poincaré sections for $TVF_{Re=153.5} + \varepsilon \times PFL$ for (a) ε=0.001 and (b) ε=0.1. Left is lower vortex, right cis close up of the inflow jet region.

KAM theory indicates that for small perturbations such as the one here, rational tori (i.e. described by periodic lines) cannot survive, breaking down into a mixture of local chaos (red points in Figure 3a) and regularity (blue and yellow structures just visible in Figure 4). In contrast, neighbouring tori that are sufficiently irrational will survive the perturbation (e.g. the red lines in Figure 4 that are cross sections of irrational tori). As the perturbation ε increases more of the outer tori are consumed and the perturbation influences the particle trajectories closer to the vortex centre. Just visible in Figure 3b (right) is the remnant of a higher-order periodic structure (red closed curve in the centre) formed as the outer tori were substantially consumed by chaos.

This transition is basically that described by KAM theory for infinitesimal flow perturbations of a 2D time-periodic flow, with the azimuthal direction here taking the place of time. This theory states that rational tori break up into island chains surrounded by chaos and irrational tori survive.

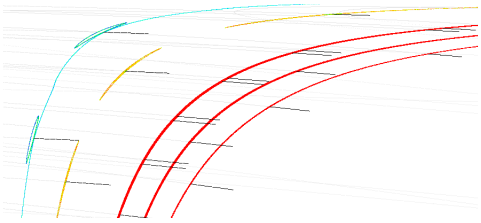

Figure 4. Close up of Poincaré sections and Period-1 lines for ε=0.001.

As the perturbation increases, more structure appears in the outer regions of the intact tori, although the perturbation distorts their shape as seen in Figure 5. Clearly seen here is an "island chain" (orange structures) that is associated with a very high-order periodic line remnant of a rational tori.

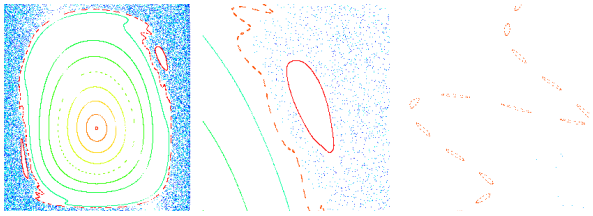

Figure 5. Close up of Poincaré sections for ε=0.5, increasing zoom from left to right..

In addition to consuming the KAM tori from the outside, the perturbation also modifies flow inside the remnant TVF vortices tori. A search for periodic lines reveals that one of the inner P1 tori has also been perturbed, leaving a set of alternating hyperbolic and elliptic points. This set of points is contained between two KAM surfaces that are so close together it is impossible to see the structure surrounding them. By stretching the radial coordinate (and unrolling the azimuthal coordinate) these are plotted in Figure 6 for $\varepsilon = 0.5$ and 0.8.

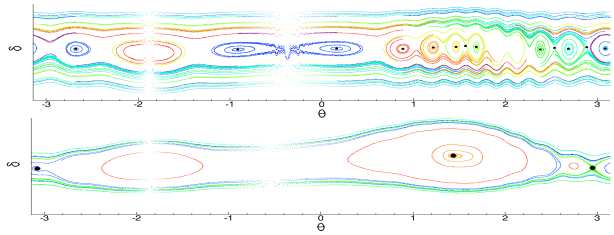

Figure 6. Poincaré sections in stretched coordinates (δ vs. θ) for $\varepsilon = 0.5$ (top) and 0.8 (bottom). The vertical axis scaling is arbitrary represents approximately 10^{-4} times cylinder gap width for $\varepsilon = 0.5$ and 10^{-2} times for $\varepsilon = 0.8$.

For $\varepsilon = 0.5$ multiple alternating elliptic and hyperbolic points are found and as the perturbation increases, these are gradually annihilated in pairs leaving just a few by $\varepsilon = 0.8$. The thickness of the region enclosing these points also expands from 10^{-4} at $\varepsilon = 0.5$ to 10^{-2} at $\varepsilon = 0.8$. By $\varepsilon = 1.0$ (Re=153.6) only a single elliptic-hyperbolic pair exists that is visible without coordinate stretching as seen in Figure 7.

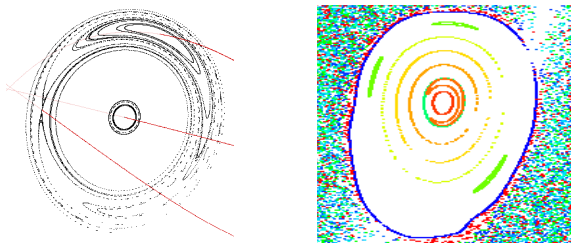

Figure 7. Poincaré section for Re=154. Close-up of inner KAM tori with 3 periodic lines (left), and wider view showing entire upper vortex.

This is seen as the (orange) reniform structure (centred on an elliptic line) that corkscrews around the central KAM tori. The hyperbolic line does not appear associated with chaotic flow, and as Re is increased beyond 154.2, these lines annihilate each other.

Prior to this point the LCSs are equivalent to those observed in the transition to chaos in unsteady 2D flows. For larger perturbations a new structure makes its first appearance as shown in Figure 8 (for ε=1.0, Re=153.6). As in the case of 2D unsteady flows, with changing perturbation new periodic points can appear in the flow in pairs, although here they are periodic lines embedded in 3D. In the Poincaré section, it appears that the outermost surviving KAM torus has bifurcated into a double homoclinic orbit (lime green) that encircles the central KAM region and two new elliptic periodic lines (each inside the small red KAM island). The true nature of this structure can be seen in a 3D stroboscopic map (the red ring-like structure in Figure 9).

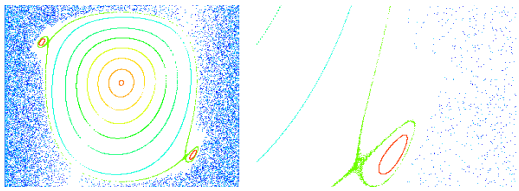

Figure 8. Poincaré section for Re=153.6 (ε=1.0).

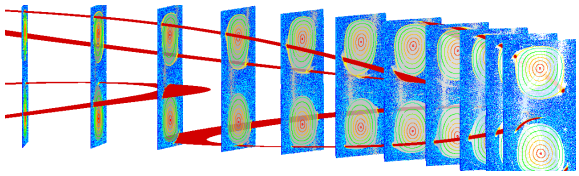

Figure 9. Stroboscopic map with multiple Poincaré sections for Re=153.6 (ε=1.0). The red ring structure seen in Figure 8 is actually a closed torus that encircles the remnants of the original TVF KAM tori.

This invariant structure is a topologically unconnected torus that encircles the original invariant KAM tori of the Taylor vortices, i.e. the remaining TVF invariant tori pass through the middle of the new structure. This is clearly seen in Figure 9 that shows multiple Poincaré sections equally spaced in θ with several of these new tori shown (in red). This kind of complex connectivity is not possible in the 2D unsteady case and is a uniquely 3D feature. As the Re increases beyond 153.6 (i.e. ε increases beyond 1), this new feature has disappeared again sometime before Re=154. A similar structure reappears around Re=154.5, this time completely separated from the remnant central KAM tori by a chaotic sea. As Re increases still further, this KAM torus grows in size (Figure 10), although itself begins to break down via a similar mechanism as the original central KAM surfaces, with higher order periodic lines being born which are themselves surrounded by KAM surfaces (see Figure 10 right).

A key point is that the transition to chaos predicted by KAM theory is here observed for flow that is well beyond the level of small perturbation where the theory is valid, and across a range of different spatial scales. It is likely that that the island chains observed in Figure 10 (lower) are destroyed in the same manner.

Eventually all of these KAM surfaces are destroyed, leaving a flow that is fully chaotic at around Re=158. The behaviour of these families of KAM tori is essentially the same as exhibited by 2D unsteady flows due to their Hamiltonian structure and implies that the 3D steady WVF can in a dynamic sense be seen as a composition of Hamiltonian systems that each correspond with a family of KAM tori and its direct environment. This is consistent with the fact that 3D steady flows admit (local) expression as a Hamiltonian system in regions anywhere outside isolated stagnation points 0

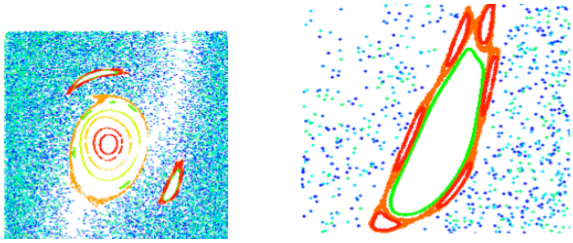

Figure 10. Poincaré section for Re=155.7. The red KAM surface again encircles the remnant central KAM surfaces and begins to break down via a similar route as the original vortices.

Conclusions

Accurately calculating LCSs in a flow that has no analytic solution is critically dependent on an ability to perform divergence-free interpolation from a discrete grid. Here we summarise a methodology for creating such fields and illustrate the improved fidelity of the results. Using this method to investigate the transition from axisymmetric TVF (at Re=153.5) to fully chaotic wavy vortex flow by Re=158, we show the transition partially follows that predicted by 2D unsteady KAM theory. The peak perturbation in TVF occurs at the inflow boundary between vortices and as it increases, the outer periodic KAM surfaces are destroyed with the gradual replacement by island chains around elliptic lines, with hyperbolic lines threading between them. This destruction leads to chaotic regions forming in the outer parts of the TVF vortices. Simultaneously, the perturbation destroys KAM surfaces well inside the original KAM region in a similar way, although does not lead to chaos there. New KAM surfaces are also born via the creation of elliptic lines that are topologically disconnected from the TVF vortices and encircle them. Such structures have no equivalent in 2D unsteady flows and highlight the new possibilities that arise in 3D flows.

Acknowledgments

MR thanks MFMS and TU/e for hosting his visit in 2015. BR and MR thank the IITB-Monash Academy and CSIRO for support.

References

[1] Andereck, C. D., Liu, S. S. and Swinney, H. L., 'Flow Regimes in a Circular Couette System with Independently Rotating Cylinders,' *J. Fluid Mech*., **164**, 155 (1986).
[2] Bajer, K., 'Hamiltonian formulation of the equations of streamlines in three-dimensional steady flows', *Chaos* **4**, 895–911 (1994).
[3] Blackburn, H. M. and Sherwin, S., 'Formulation of a Galerkin spectral element-Fourier method for 3D incompressible flows in cylindrical geometries', *J. Comput. Phys.* **197** 759-778 (2004).
[4] Coles, D., 'Transition in Circular Couette Flow', *J. Fluid Mech*., **21**, 385 (1965).
[5] Finn, J. M. and Chacon, L., 'Volume preserving integrators for solenoidal fields on a grid', *Physics of Plasmas* **12** 1-4 (2005).
[6] Grebogi, C., Hammel, S.M., Yorke, J.A. and Sauer, T., 'Shadowing of physical trajectories in chaotic dynamics: Containment and refinement', *PRL*. **65** 1527-1530 (1990).
[7] Haller, G. 'Lagrangian coherent structures', *Ann. Rev. Fluid Mech.* **47** 137-162 (2015).
[8] Ottino, J.M., *The kinematics of mixing: stretching, chaos, and transport*, Cambridge University Press (1989).
[9] Ravu, B., Rudman, M., Metcalfe, G. P., Lester, D. R. and Khakhar, D.V., 'Creating analytically divergence-free velocity fields from grid-based data', *J. Comput. Phys.* **323** 75-94 (2016).
[10] Rudman, M., 'Mixing and particle dispersion in the wavy vortex regime of Taylor-Couette flow', *AIChE J.* **44** 1015-1026 (1998)